Chinese Journal of Chemical Engineering 53 (2023) 89–100

Contents lists available at ScienceDirect

Chinese Journal of Chemical Engineering

journal homepage: www.elsevier.com/locate/CJChE

Full Length Article

Towards superior permeability and antifouling performance of sulfonated polyethersulfone ultrafiltration membranes modified with sulfopropyl methacrylate functionalized SBA-15

Eid H. Alosaimi [1], Ibrahim Hotan Alsohaimi [2,*], Hassan M.A. Hassan [2], Qiao Chen [3], Saad Melhi [1], Ayman Abdelaziz Younes [1]

[1] Department of Chemistry, College of Science, University of Bisha, Bisha 61922, Saudi Arabia
[2] Chemistry Department, College of Science, Jouf University, Sakaka 2014, Saudi Arabia
[3] Chemistry Department, School of Life Sciences, Sussex University, Brighton BN1 9QJ, UK

ARTICLE INFO

Article history:
Received 26 July 2021
Received in revised form 24 September 2021
Accepted 27 September 2021
Available online 12 October 2021

Keywords:
Ultrafiltration membrane
Antifouling
Permeability
SBA-15
NOM foulant

ABSTRACT

A non-solvent induced phase separation (NIPS) process was used to fabricate a series of sulfonated polyethersulfone (SPES) membranes blending with different concentrations of SBA-15-*g*-PSPA with the applications in the ultrafiltration (UF) process. SBA-15 was modified with 3-methacrylate-propyltrime thoxysilane (MPS) to form SBA-15-*g*-MPS. It was further modified with the charge tailorable polymer chains by reacting with 3-sulfopropyl methacrylate potassium salt. The nanoparticles were uniformly dispersed and finger-like channels were developed within the membrane. The adding of surface modified SBA-15-*g*-PSPA nanoparticles has significantly improved membrane water permeability, hydrophilicity, and antifouling properties. The pure water fluxes of the composite SPES membranes were significantly higher than the pristine SPES membrane. For the membrane containing 5% (mass) of SBA-15-g-PSPA (MSSPA5), the pure water flux was increased dramatically to 402.15 $L{\cdot}m^{-2}{\cdot}h^{-1}$, which is ~1.5 times that of MSSPA0 (268.0 $L{\cdot}m^{-2}{\cdot}h^{-1}$). The high flux rate was achieved with 3% (mass) of SBA-15 nanoparticles with retained high rejection ratio 98% for natural organic matter. The results indicate that the fashioned composite membrane comprising SBA-15-*g*-PSPA nanoparticles have a promising future in ultrafiltration applications.

1. Introduction

Water demand has risen significantly in recent years as a result of population and economic growth, resulting in extreme freshwater shortages. Since humans can only utilize 0.007% of the water on earth, water recycling is now one of the most pressing concerns [1]. As a result, membrane technology has progressed rapidly in the sector of water separation and cleaning. Due to its eco-friendliness, low-energy consumption, low chemical consumption, reduced secondary contamination, and simplicity of use, the ultrafiltration (UF) membrane technique is commonly applied as a green wastewater-regeneration and treatment technique [2–5]. Polymer-based UF membranes with easily engineered unique morphology, internal structures, and surface properties play a significant role in ultrafiltration technology. Membrane fouling is originated from attractive columbic intermolecular force between the organic pollutants and the membrane surface. Hence, polymer-based UF membranes with antifouling property can be developed by controlling the surface property [6,7]. Hydrophilic membranes will be less exposed to the fouling by natural organic matter (NOM) due to reduced adhesion of the hydrophobic foulant and the hydrophilic surface of the membrane. A functionalized membrane with a hydrophilic surface and large surface tension can also improve the hydrogen bond formation with the surrounding water molecules. Such a layer of water helps to minimize and inhibit foulants accumulate on the membrane surface [8–10]. The surface sulfonation technique was frequently used to modify polymer membrane surfaces, primarily because the sulfonic acid moiety is hydrophilic and the coupling reaction process is simple [11–15]. However, with more sulfonic acid groups incorporated into the polymers matrix, the mechanical strength and the thermal stability of the membranes will decrease. Large sulfonic acid groups can induce extreme swelling, which would affect mem-

* Corresponding author.
E-mail address: ehalshaimi@ju.edu.sa (I.H. Alsohaimi).

https://doi.org/10.1016/j.cjche.2021.09.019
1004-9541/

brane rejection [16]. Hence, delicate control in the improving of the membrane's hydrophilicity without sacrificing other characteristics, particularly rejection, has become a major challenge. Surface coating [17–25], grafting [26], and blending [27] are the most common methods used for chemically modifying the surface property of a membrane. While the efficiency of the membranes can be enhanced without losing their intrinsic mechanical properties, those surface modifications can also result in a reduction in permeability, which should be addressed. Alternatively, the adding of inorganic and metallic nanoparticles in the surface coating could help to maintain the permeability. Different nanoparticles, such as metallic silver [28–30], graphene oxide [31,32], TiO_2 [33], and zinc oxide [34], were utilized as the membrane fillers. For example, Zhang *et al.* [35] synthesized polyethersulfone (PES) UF membranes with added composite nanoparticles of SiO_2/hydrolyzed polyacrylonitrile, achieving a water flux of 354 $L{\cdot}m^{-2}{\cdot}h^{-1}$ and bovine serum albumin (BSA) rejection ratio of 94%.

Mesoporous materials were commonly used in adsorption, separation, and catalysis [36]. SBA-15 is highly ordered 2-D hexagonal mesoporous silica. Due to its strong mechanical and thermal stability, high density surface silanol moieties (SiOH), large surface area, and narrow pore size distribution [37], it is one of the most intensively studied materials. For instance, Martín *et al.* [38] fabricated the PES/SBA-15 composite with increased water permeation while maintaining membrane selectivity. Although increasing the membrane's hydrophilicity will increase its antifouling and permeability, the lack of compatibility between polymers and nanoparticles remains a challenge for developing high quality, stable and homogeneous distributed composite materials [39–43].

This study aims to prepare polymer chains-grafted SBA-15 to enhance the interaction with polymer matrix and prevent nanofiller aggregation, resulting in high permeability hybrid UF porous membranes. In this work, a charge-controllable polymer-silica composite (SBA-15-*g*-PSPA) was fabricated *via* the reaction of 3-sulfopropyl methacrylate potassium salt with 3-methacrylate-propyltrimethoxysilane (MPS) functionalized SBA-15 (SBA-15-*g*-MPS). The SBA-15-*g*-PSPA was added to the sulfonated PES to form the composite material for the UF membrane. The strong columbic interaction helps to enhance the coupling between the inorganic nanoparticles and the PES polymer matrix. Meanwhile, the membrane hydrophilicity was significantly enhanced with the introduction of sulfonic acid moieties, which is favourable to the membrane rejection ratio and permeability. Furthermore, the effects of SBA-15 addition on the membrane mechanical property, hydrophilicity, morphologies, permeability, and antifouling characteristics were systematically investigated.

2. Experimental

2.1. Materials

Polyethersulfone (PES, M_w 58000 $g{\cdot}mol^{-1}$) was obtained from Goodfellow, USA. Pluronic surfactant (P-123, average $M_w \sim 5800$ $g{\cdot}mol^{-1}$), tetraethyl orthosilicate (TEOS, 98%), ethanol (99%), hydrochloric acid (HCl, 37%), sodium hydroxide (NaOH, ≥98%), 3-sulfopropyl acrylate potassium salt (SPA), polyvinylpyrrolidone (PVP), ethylene glycol dimethacrylate (EGDMA, 98%), azobisisobutyronitrile (AIBN, 98%), 3-methacrylate-propyltrimethoxysily (MPS, 98%), calcium chloride ($CaCl_2{\cdot}2H_2O$, 98%), sodium chloride (NaCl, ≥99.5%), bovine serum albumin (BSA, ≥98%), *N*-methyl-2-pyrrolidinone (NMP, ≥99%), *N*,*N*-dimethylformamide (DMF, ≥99.5%), humic acid (HA), and alginic acid sodium salt (SA, ≥99.5%) were procured from Sigma-Aldrich Co., USA. H_2SO_4 (96%) used for sulphonation of PES was obtained from Fisher Scientific. All chemicals were used as obtained together with ultra-pure water, provided by a Millipore Milli-Q Direct 8 purification system (Millipore, France). The NOM solution was prepared according to the literature [44]. The solution contains 10 $mg{\cdot}L^{-1}$ (each) of BSA, SA, and HA, 1 $mmol{\cdot}L^{-1}$ $CaCl_2$ and 7 $mmol{\cdot}L^{-1}$ NaCl in DI water.

2.2. Materials fabrication

2.2.1. SBA-15 synthesis

Silica SBA-15 was synthesized with the standard sol–gel method employing TEOS as the silica source and Pluronic P123 as structure directing agent (SDA) [37]. Good quality meso-silica of SBA-15 was obtained after calcined for 6 h at 550 °C to remove the SDA.

2.2.2. Synthesis of modified SBA-15 (SBA-15-g-MPS)

To prepare the modified SBA-15, 1.5 ml MPS and 10 mg SBA-15 were evenly dispersed in 10 ml ethanol with 60 min sonication, followed by 16 h vigorous stirring at 50 °C. The precipitate was rinsed with ethanol several times before centrifuged. The collected SBA-15-*g*-MPS powder was dried at 30 °C under vacuum (Fig. 1).

2.2.3. Synthesis of SBA-15-g-PSPA

Using the free-radical polymerization approach, the SBA-15-*g*-PSPA was prepared using AIBN as the initiator and EGDMA as the cross-linker. A 500 ml 2-neck round bottom flask was connected with a reflux condenser, which contained 40 mg SBA-15-*g*-MPS dispersed in 100 ml acetonitrile. The mixture was sonicated for 30 min before 0.5 g EGDMA, 0.5 g SPA, and 20 mg AIBN were introduced into the dispersed solution. To complete the free-radical polymerization, the solution was refluxed for 2 h at 95 °C. The product, SBA-15-*g*-PSPA, was washed with water and ethanol. The sample was collected *via* centrifugation followed by drying at 80 °C under vacuum for 24 h (Fig. 1).

2.2.4. Fabrication of SPES/SBA-15-g-PSPA composite membrane

A nonsolvent induced phase separation (NIPS) method was adopted for the fabrication of the UF membranes. The detailed process is shown in Fig. 2. Typically, SBA-15-*g*-PSPA composite was dispersed in NMP by sonication for 60 min until a homogenous suspension was obtained. Subsequently, SPES (sulfonated polyethersulfone, 18% (mass)) and PVP (2% (mass)) (The method for the synthesis of SPES is described in the Supplementary Material) were introduced into the SBA-15-*g*-PSPA suspension slowly under continuous stirring at 350 $r{\cdot}min^{-1}$ at 50 °C for 3 h. PVP was introduced to the casting solutions as a hydrophilic additive. In order to achieve a good composite dispersion, the mixture was stirred for another 24 h at similar temperature. Before casting the membrane, the polymer solution was sonicated for 20 min and kept standstill to remove air bubbles. The solution was cast on a clean glass using a casting knife with a film thickness of 250 μm. The sample was then dried in air for 20 s before being settled by soaking the support plate with the polymer film into a precipitation bath of water as the nonsolvent. The samples were left in the nonsolvent bath for few minutes to achieve a full exchange of solvent and nonsolvent, which resulted in the membrane detaching from the glass support. The obtained membrane was rinsed with deionized water to remove the residual solvent. The membrane mass composition with 1%, 3%, and 5% SBA-15-*g*-PSPA donate as MSSPA1, MSSPA3, and MSSPA5 respectively (Table 1). For comparison, a pristine membrane (MSSPA0) without SBA-15-*g*-PSPA was also prepared.

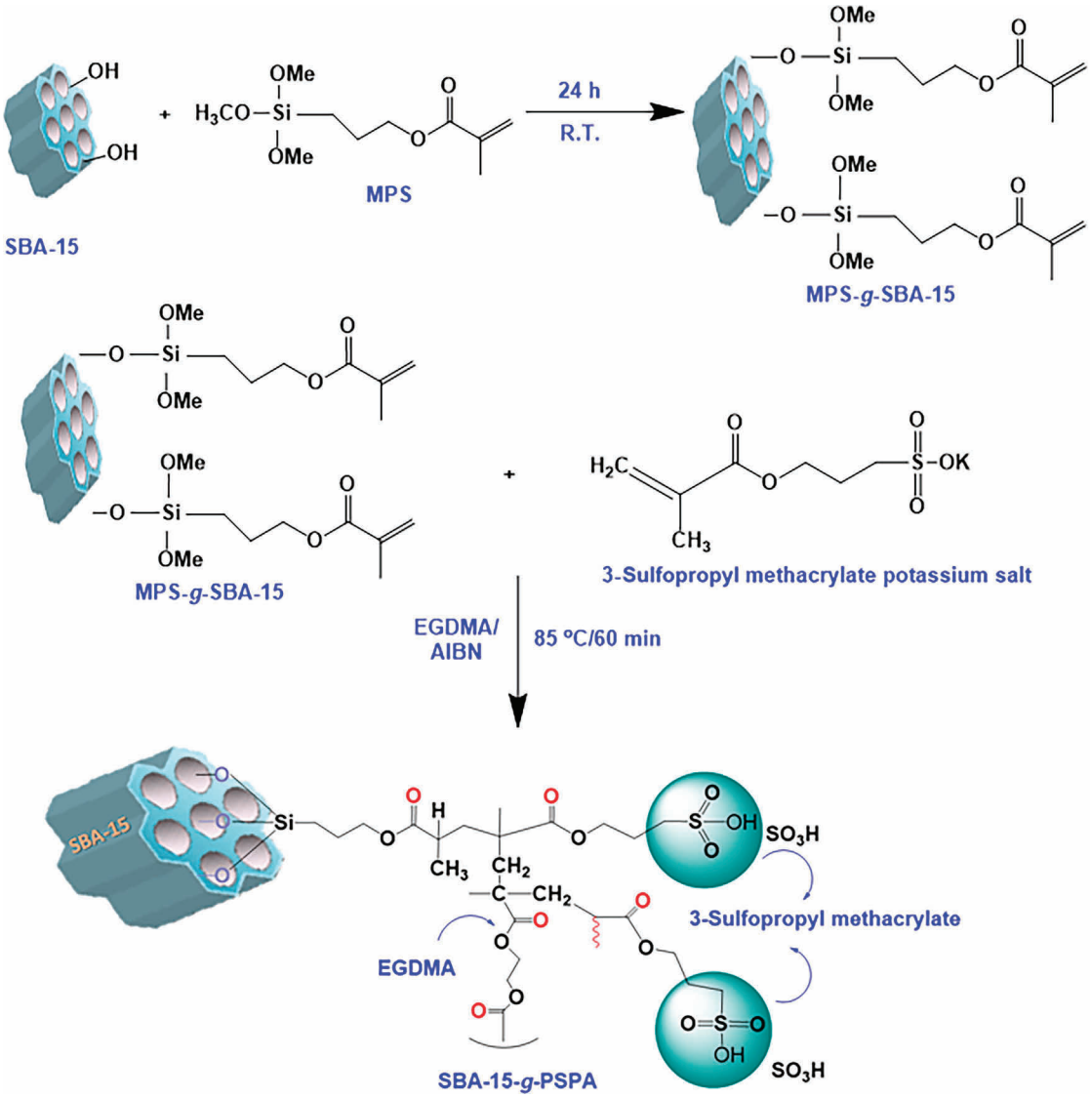

Fig. 1. Schematic illustration for the synthesis of SBA-15-*g*-PSPA.

2.3. Composite membranes characterization

Fourier transform infrared spectroscopy (FT-IR) was collected on IR Tracer-100 FTIR spectrophotometer (Shimadzu, Japan) with a scan range from 4000 to 400 cm^{-1}. The crystal structures were studied with a powder X-ray diffractometer (XRD, Optima7000, Shimadzu) using the Cu K_α radiation (λ = 0.15406 nm). Thermal gravimetric analysis (TGA, STA-449F3, Shimadzu) was performed in N_2 gas from 50 to 600 °C at a heating rate of 10 °C·min^{-1}. The ^{29}Si NMR spectra were collected from an NMR instrument (RESONANCE, JEOL, Japan). The top surface and cross-section morphologies of the fabricated membranes were investigated by field emission scanning electron microscopy (FESEM, Thermo Scientific Quattro ESEM, Thermo Fisher, USA). Tensile assessment was conducted using a tensile tester Shimadzu EZ-S. The membrane hydrophilicity was assessed by measuring the water contact angles using a SCA20 Goniometer (Data Physics, USA) fitted with a digital camera. The zeta potential was evaluated employing an electrokinetic analyzer for solid surface analysis (SurPASS, Anton PaarGmbH, Austria).

The porosity (ε) of the fabricated membrane was performed as follows. Membrane sheets (2 cm^2) were weighted, they have been submerged in deionized water at ambient temperature for 24 h. The wet membrane sheets were vacuum dried at 60 °C for 12 h before being weighted. The porosity (ε) of the membrane was calculated using Eq. (1):

$$\varepsilon = \frac{W_1 - W_2}{A t_h \rho} \tag{1}$$

where W_1 and W_2 are the mass of the wet and dry membranes, respectively. A is the membrane area; t_h is the thickness and ρ is the water density.

The mean pore radius (r_m) was determined using the Guerout–Elford–Ferry *via* Eq. (2):

$$r_m = \sqrt{\frac{(2.9 - 1.75\varepsilon)8\mu t_h Q}{\varepsilon A \Delta P}} \tag{2}$$

where μ is the viscosity of water (8.9×10^{-4} Pa·s), t_h is the membrane thickness, Q is the permeate pure water volume ($m^3 \cdot s^{-1}$) and ΔP is the applied pressure.

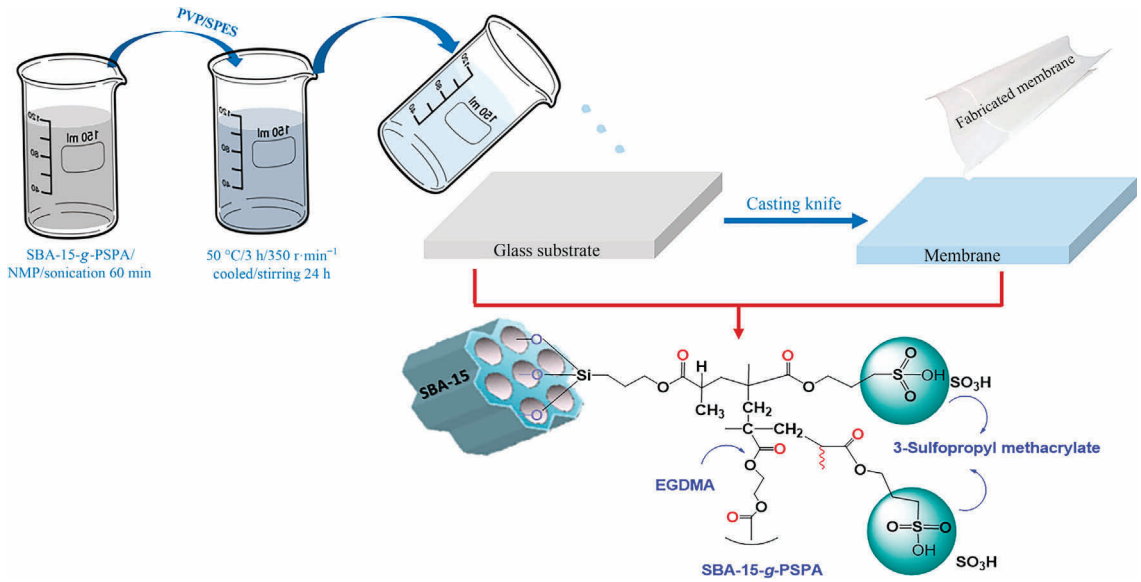

Fig. 2. Schematic illustration for the casting processes of the membrane.

Table 1
The mass composition of casting solutions

Membrane	SPES/%	PVP/%	SBA-15-*g*-PSPA[①]/%	NMP/%
MSSPA0	18	2	0	80.00
MSSPA1	18	2	1	79.64
MSSPA3	18	2	3	79.28
MSSPA5	18	2	5	79.10

① The percentage of SBA-15-*g*-PSPA is based on the total fraction of SPES polymer in the casting solution.

2.4. Ultrafiltration experiments

The UF experiments have been tested using a stirred dead-end UF cell (Amicon 8050; Millipore). Each membrane was pre-tested with deionized water at 2×10^5 Pa for 30 min to make sure no cracks or leakages. The ultrafiltration tests were run at 10^5 Pa. The mass of permeate in 30 min was measured. Eq. (3) was utilized to assess the pure water flux, J_w:

$$J_w = \frac{m}{\rho A t} \tag{3}$$

where m is the permeate mass, A is the membrane area, and t is the permeation time. The water flux measured from a pristine membrane is defined as J_{w1}. Subsequently, the prepared foulant solutions (100 μg·g^{-1} of SA, HA, and BSA, and authentic NOM) [45] were introduced at 10^5 Pa. The permeation flux of the foulants solutions (J_F) was also estimated using Eq. (3). The foulant rejection ratio (R) was calculated by following Eq. (4):

$$R = \left(1 - \frac{C^t_{permeate}}{C^o_{feed}}\right) \times 100\% \tag{4}$$

where C^o_{feed} and $C^t_{permeate}$ are the concentrations of foulant in the feed and permeate. After the measurement, the membrane was washed with DI water and 0.02 mol·L^{-1} NaOH solution to remove the adsorbed foulants. The pure water flux of the washed membrane (J_{w2}) was evaluated for another 30 min. To emphasize the antifouling efficiency, flux recovery ratio (FRR), the total fouling ratio (R_t), reversible fouling ratio (R_r) and irreversible fouling ratio (R_{ir}) were calculated *via* Eqs. (5)–(8).

$$FRR = \frac{J_{w2}}{J_{w1}} \times 100\% \tag{5}$$

$$R_t = \frac{J_{w1} - J_F}{J_{w1}} \times 100\% \tag{6}$$

$$R_r = \frac{J_{w2} - J_F}{J_{w1}} \times 100\% \tag{7}$$

$$R_{ir} = \frac{J_{w1} - J_{w2}}{J_{w1}} \times 100\% \tag{8}$$

The foulant concentrations in water were measured with a UV–vis spectrometer (Cary 60, Agilent, USA). The adsorption capacity per unit area of the membrane (q) was evaluated using Eq. (9) [27–29].

$$q = \frac{(C_o - C_t)V}{A} \tag{9}$$

where V and A are the solution volume and the actual membrane area used in the adsorption experiments; C_o and C_t are the foulant concentrations at the beginning and the end of the filtration.

3. Results and Discussion

3.1. Characterization of SBA-15 and SBA-15-g-PSPA

Fig. 3(a) reveals the FT-IR spectra of the prepared SBA-15 (inset) and SBA-15-*g*-PSPA composite. For the pristine SBA-15 sample, the symmetric and asymmetric stretching bands of Si—O—Si modes at 806 and 1083 cm^{-1} was observed [37,46,47]. The characteristics band at 470 cm^{-1} is attributed to the bending mode of the Si—O—Si, while the band at 967 cm^{-1} is associated with the asymmetry mode of the surface Si—OH moieties. The absorption band at 1631 cm^{-1} is due to the bending modes of the Si—OH moieties. The strong and broad absorption band 3441 cm^{-1}, is assigned to the stretching vibration of surface OH moieties. The FTIR spectrum of the bare SPES is described in the Supplementary Material.

Compared to the pristine SBA-15, the intensity of bands related to Si—OH and —OH were reduced significantly in SBA-15-*g*-PSPA. Besides, new absorption bands were observed at 1044, 1165, 1395, 1454, 1725, 2340, and 2948 cm^{-1}, assigned to symmetric

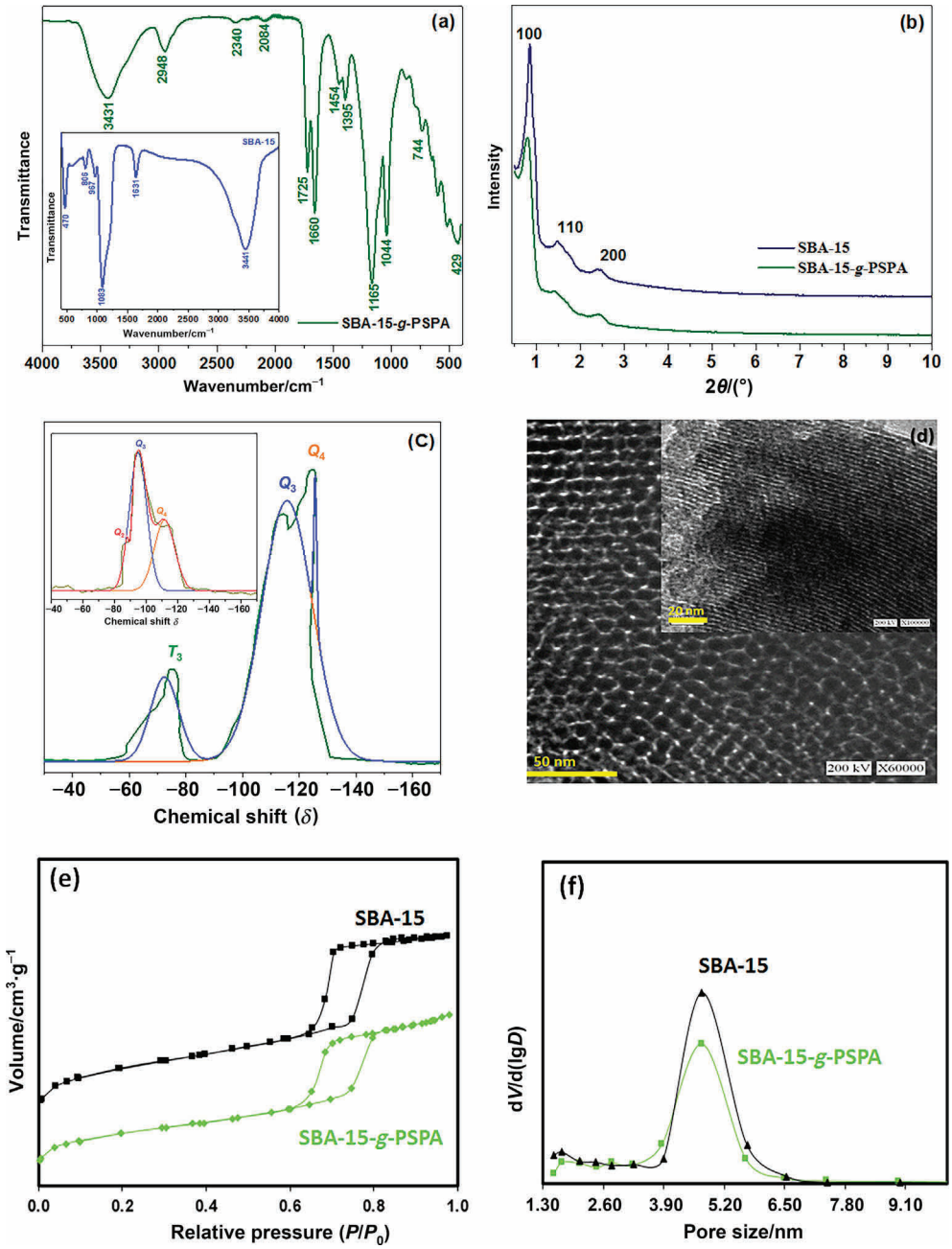

Fig. 3. (a) FTIR spectra, (b) low angle XRD, (c) solid state ^{29}Si NMR, of pure SBA-15 (inset) and functionalized SBA-15, and (d) HRTEM of SBA-15, the synthesized SBA-15-*g*-PSPA composite (inset), (e) Nitrogen isotherms at −196 °C, and (f) pore size distribution of SBA-15-*g*-PSPA composite.

O═S═O stretching, asymmetric O═S═O stretching, —CH_2— vibration, —CH_3 moieties, C═O stretching, and —CH_2 moieties stretching vibration. The change of the FTIR spectrum affirms the successful modification of the SBA-15 surface through the grafting of EGDMA with MPS.

The low-angle XRD patterns for SBA-15 and SBA-15-*g*-PSPA composite are displayed in Fig. 3(b). Both samples presented similar diffraction patterns with three diffraction peaks associated with the (1 0 0), (1 1 0), and (2 0 0) crystal planes of P6mm hexagonal symmetry of the silica framework. It confirms that the long-order mesoporous hexagonal structure was maintained after the surface functionalization [46].

The solid state ^{29}Si NMR for SBA-15 and SBA-15-*g*-PSPA composite are depicted in Fig. 3(c). The spectrum of SBA-15 (inset in Fig. 3(c)) displays three distinct resonance at δ −86, −94, and −110 assigned to geminal silanol (Q_2), single silanol (Q_3), and siloxane (Q_4) sites of the silica matrix, respectively [28,29]. Upon the SBA-15 functionalization, the Q_2 signal vanished and the Q_3 signal weakened, while the Q_4 signal became stronger. Furthermore, a new peak at δ −75.15 was appeared, which is ascribed to the T_3 signal, which indicates the successful incorporation of organic functionalities. The incorporation of the functionality into SBA-15 materials happens by grafting between silica surface silanol groups and 3-methacrylate-propyltrimethoxysily. These findings suggested that the isolated and geminal Si—OH groups were consumed during the functionalization process. Furthermore, it's obvious that the fabricated SBA-15-*g*-PSPA nanoparticle displayed well-ordered mesoporous structures (inset in Fig. 3(d)). Besides, the morphology of the SBA-15 nanofiller was remained unchanged after the modification process. FESEM (Supplementary Material)

and HRTEM investigations confirm that the SBA-15 have the same morphology after the modification process.

As displayed in Fig. 3(e), based on IUPAC classification, the N_2 adsorption–desorption isotherms of SBA-15 possess a type IV isotherm. An obvious hysteresis loop of mesoporous materials is obtained. The BET surface area was 880.23 $m^2 \cdot g^{-1}$, and the total pore volume was 1.58 $cm^3 \cdot g^{-1}$ with narrow pore size distribution centred at 6.3 nm in Fig. 3(f). A similar test of SBA-15-g-PSPA was carried out. In Fig. 3(e) and (f), SBA-15-*g*-PSPA has a typical mesoporous structure and its pore size of the adsorption branch was 6.2 nm with a narrow pore size distribution. The BET surface area was 650.14 $m^2 \cdot g^{-1}$, and the total pore volume was 1.34 $cm^3 \cdot g^{-1}$. Because the functionalization of SBA-15 caused partial pore collapsed, made BET surface area and pore volume became smaller.

3.2. Membrane characterization

The FTIR spectra of membrane samples with different SBA-15 contents are displayed in Fig. 4(a). The characteristics peaks at 867 and 1020 cm^{-1} are accredited to the O—Si stretching vibrations, respectively. The bands at 1095 and 1156 cm^{-1} are assigned to O═S═O stretching vibration. The absorption band at 1243 cm^{-1} is ascribed to the vibration of –O-moiety. The vibration peaks associated with the aromatic rings are assigned to the characteristics bands at 1485 and 1575 cm^{-1}. The peak at 1677 cm^{-1} is assigned to the C═O stretching and the band at 2965 cm^{-1} is related to C—H stretching. Thus, the FTIR confirms the successful fabrication of SPES/SBA-15-*g*-PSPA composite membranes.

XRD was also used to investigate the incorporation of inorganic nano-filler in the polymer matrix, shown in Fig. 4(b). The MSSPA0 shows a broad diffraction peak at 26.1°, which is typical for SPES membrane. By adding SBA-15-*g*-PSPA, an additional peak at 18.2° appeared which is overlapped with the diffraction peak from SPES, due to their peak broadness. With the increase in the SBA-15-*g*-PSPA contents, the peaks have a much smaller intensity after the addition of silica nanofiller to the polymer matrix, suggesting a disordered meso structure and a clear diverse impact of SPES on the nanofiller. Moreover, a small intense peak was also observed at 42.2° due to the grafting of mesoporous silica within the polymer matrix.

TGA was used to measure the membrane thermal stability, shown in Fig. 4(c). All the materials showed a two-stage mass loss process: (i) a mass-loss stage observed at a temperature below 180 °C related to the loss of physiosorbed water. (ii) a peak in the temperature range of 200–414 °C, which attributed to the degradation of carboxyl moieties. The remaining organic components, including the residual polymer main chain, decomposed as the temperature increased. With the addition of SBA-15-*g*-PSPA, the leading decomposition temperature is greater than the pristine membrane, suggesting an enhancement in the thermal stability with incorporating mesoporous silica.

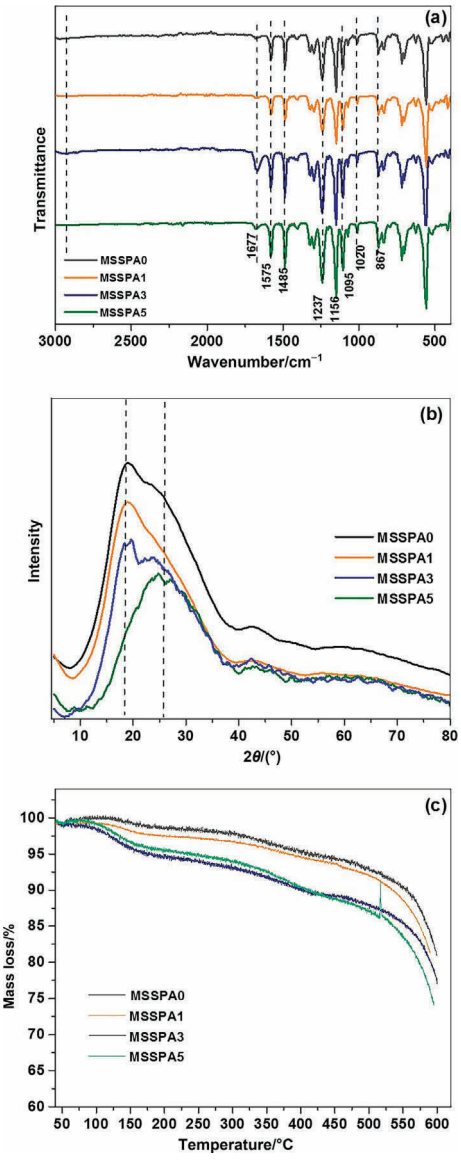

Fig. 4. (a) ART-FTIR spectra, (b) wide angle XRD, and (c) TGA profiles in the temperature range from 30 to 600 °C of the synthesized membranes.

3.3. Membrane surface charge

The membrane surface charge was determined by testing the surface potential (ζ) at pH equal to 7, shown in Fig. 5. Negative surface ζ-potentials were observed for all the membrane samples, due to the existence of a large concentration of —SO_3H moieties in the SPES polymer. The measured surface ζ-potentials are listed in Table 2. With the increase of the added SBA-15-*g*-PSPA, the surface ζ-potentials became more negative, depicted in Fig. 5, due to the improvement in the negatively charged hydroxide (—OH) moieties in the membrane matrix. The greatest negative surface ζ-potential

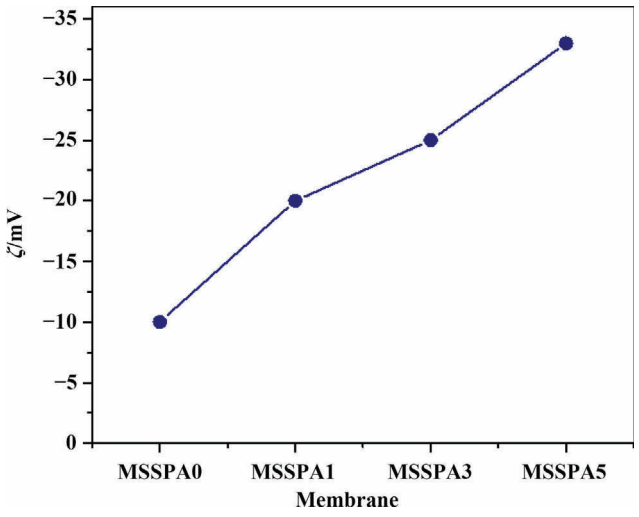

Fig. 5. The surface ζ potential of hybrid membranes with varied content of SBA-15-*g*-PSPA at pH = 7.

Table 2
The surface potential, ζ; the porosity, ε; water uptake, φ; mean pore radius, r_m; and mechanical properties mean of the fabricated hybrid membranes

Membrane	ζ/mV	ε/%	φ/%	r_m/nm	Tensile strength/MPa	Young's modulus/GPa	Elongation/%
MSSPA0	−10.1 ± 0.1	70.3 ± 0.5	65.9 ± 0.3	8.12 ± 0.1	39.1 ± 0.1	8.6 ± 0.3	3.2 ± 0.2
MSSPA1	−20.0 ± 0.1	77.6 ± 0.3	71.1 ± 0.2	14.4 ± 0.1	40.2 ± 0.3	9.2 ± 0.2	3.9 ± 0.1
MSSPA3	−25.2 ± 0.2	82.3 ± 0.2	75.1 ± 0.1	15.7 ± 0.2	42.4 ± 0.2	9.7 ± 0.1	4.6 ± 0.2
MSSPA5	−33.3 ± 0.1	81.4 ± 0.7	78.6 ± 0.2	13.6 ± 0.2	45.8 ± 0.1	10.2 ± 0.2	5.4 ± 0.2

of −33 mV was achieved with the highest contents of SBA-15-*g*-PSPA (MSSPA5). The monotonic trend of the surface ζ-potential as a function of the SBA-15-*g*-PSPA contents indicates that the hybrid membranes surface charge could be quantitatively controlled by adjusting the quantity of the SBA-15-*g*-PSPA component in the polymeric solutions.

3.4. Membrane morphology and structural properties

FESEM was employed to examine the membrane morphologies, with representative surface and cross-sectional images, illustrated in Fig. 6. The top surfaces (left images) of the membranes displayed a compact and smooth morphology with no visible defects. The

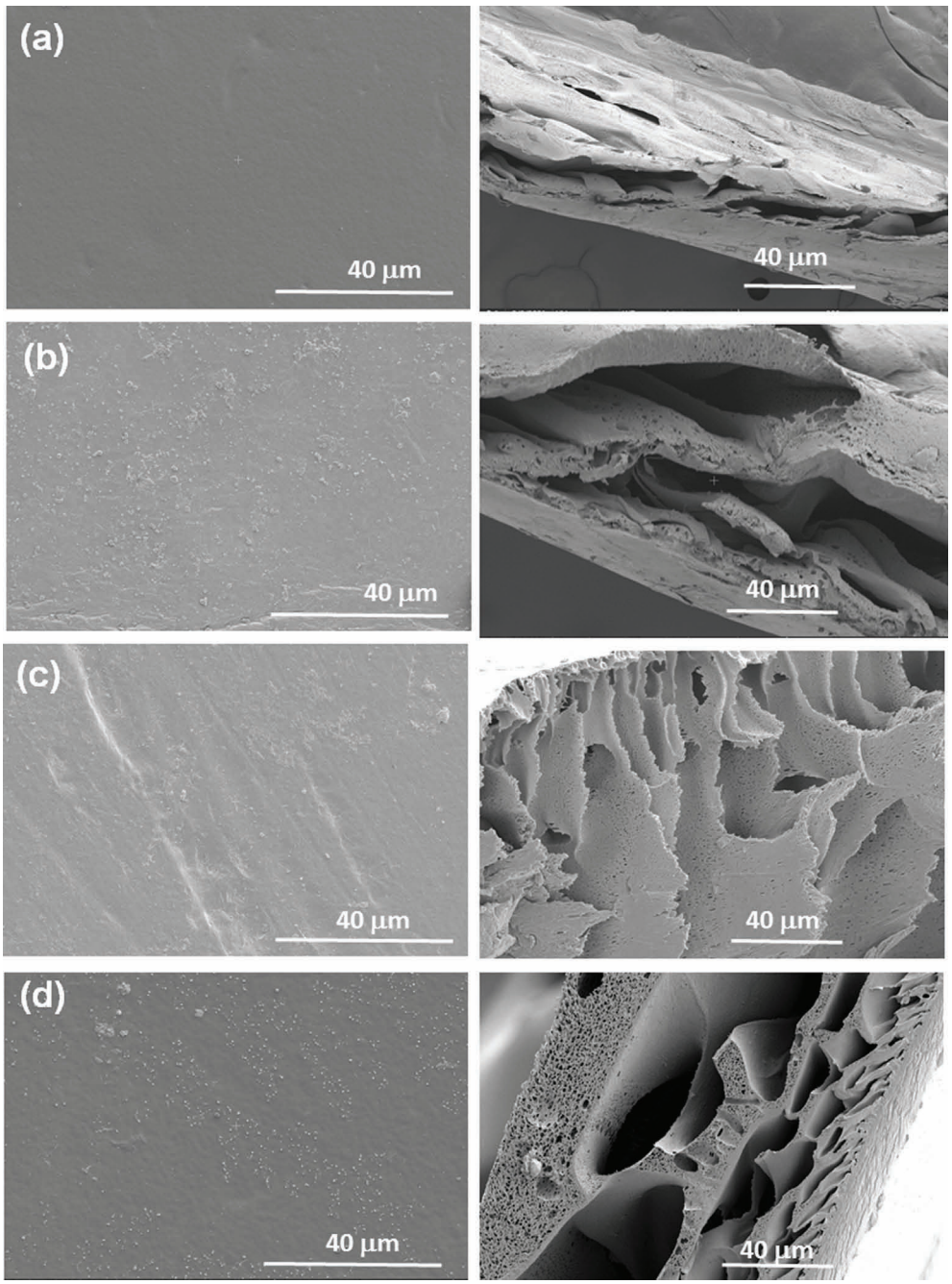

Fig. 6. The surface and cross-sectional FESEM images of the hybrid membranes: (a) MSSPA0; (b) MSSPA2; (c) MSSPA4; and (d) MSSPA5.

most of the filler nanoparticles were distributed evenly on the top surface of the fabricated membrane, which is essential for improving the membranes rejection efficiency. The pores density over the surface of the membrane increases with the mass content of SBA-15-*g*-PSPA up to 3%, then declines at 5% loading. The cross-section SEM images (right images) depict the typical irregular structure with a dense porous layer and finger-like pores on the top. The cross-sectional sublayer structure of the membrane altered after loading the SBA-15-*g*-PSPA to the polymer matrix. In contrast to the pristine membrane MSSPA0, the composite membranes (MSSPA1 and MSSPA3) have larger finger-like pores. Due to the thicker skin layer, it is expected that the pristine membranes have lower permeability with a higher rejection ratio during the ultrafiltration process. Meanwhile, the average pore sizes of the composite membranes are greater than that of the pristine membrane. This could be attributed to the fast mass transfer between the casting solution and the nonsolvent, which results in the rapid breakdown of the casting solution during the development of the membrane. This will create large groove structures within the membranes. The creation of "voids" that enable water molecules to move through is promoted by these formed finger-like channeled structures. All membranes with the addition of SBA-15-*g*-PSPA had higher porosities with larger pore radius relative to the pristine SPES membrane, shown in Table 2. This confirms that SBA-15-*g*-PSPA can accelerate the phase separation process, which is responsible for producing larger pores within the SPES, resulting in expected higher permeability and higher quantity of water uptake. The high hydrophilicity of SBA-15-*g*-PSPA is likely to be the driving force for the acceleration of the exchange between the organic solvent and nonsolvent (water) during the NIPS process. It could also weaken the stacking ordering of the SPES chains, allowing more available pores to form within the matrix of the membrane. The quantitative results are summarized in Table 2. The maximum porosity and mean pore radius of the synthesized membranes was achieved with the addition of 3% (mass) of SBA-15-*g*-PSPA. By further increase the SBA-15-*g*-PSPA mass loading to 5% (MSSPA5), the porosity was reduced. This is most likely due to a large increase in the casting solution's viscosity, which inhibits the solvent and nonsolvent exchange. Such findings were supported by the FESEM studies, shown in Fig. 6. With the addition of SBA-15-*g*-PSPA, the water uptake was increased with respect to that of the pristine membrane (MSSPA0), due to the hydrophilicity enhancement as well as the membrane porosity. The improved surface hydrophilicity of the UF membrane is important for a good water flux while maintaining a good rejection ratio.

3.5. Membrane hydrophilicity

To verify the influence of SBA-15-*g*-PSPA on the surface character of the SPES membrane, the hydrophilicity of the membrane was directly evaluated by measuring the dynamic and static contact angle, displayed in Fig. 7(a) and (b). When the amount of SBA-15-*g*-PSPA was increased, the dynamic contact angle of the hybrid membranes decreased monotonically, shown in Fig. 7(a), suggesting the membrane surface became more hydrophilic. Meanwhile, the static water contact angles, shown in Fig. 7(b), declined from 68° of MSSPA0 to 59.6° of MSSPA1. The smallest static contact angle of 40.23° was attained for the MSSPA5 membrane, with the greatest quantity of SBA-15-*g*-PSPA. The increase in the hydrophilicity with the increased concentration of SBA-15-*g*-PSPA is due to the two combined effects: 1) SBA-15-*g*-PSPA was distributed homogeneously in the membrane composite. With the increase in the SBA-15-*g*-PSPA concentration, its surface concentration will also increase. 2) The density of the surface sulfonic group will increase, which is hydrophilic. These groups have a great capability to uptake water molecules through dipole–dipole attractive interactions and hydrogen bonds. Hence, the hydrophilicity of the membrane surface, as well as the wall of the pore structure, will increase when the concentration of SBA-15-*g*-PSPA increases. As a result, the surface free energy ($-\Delta G_{SL}$) of the membranes was improved [48].

3.6. Mechanical properties

Different mechanical parameters, comprising tensile strength, Young's modulus and elongation, of the synthesized membranes using various SBA-15-*g*-PSPA concentrations, are shown in Fig. 8 and presented in Table 2. The results emphasize that tensile strength, Young's modulus and elongation, improved significantly with increased SBA-15-*g*-PSPA concentration. These increased mechanical strengths can be due to the reinforcement interaction effect of the finely distributed SBA-15-*g*-PSPA in the polymer matrix as a result of the interaction between SPES and SBA-15-*g*-PSPA. The heavy interaction improves both distribution and interfacial adhesion, significantly improving the mechanical properties of the matrix. Besides, as displayed in Table 2, it is clearly observed that the values of Young's modulus, elongation (%) and tensile strength for all synthesized membranes were greater than that obtained for the pristine membrane MSSPA0. The ability of the SBA-15-*g*-PSPA to disperse within the SPES matrix and the strong columbic interaction between them are responsible for the

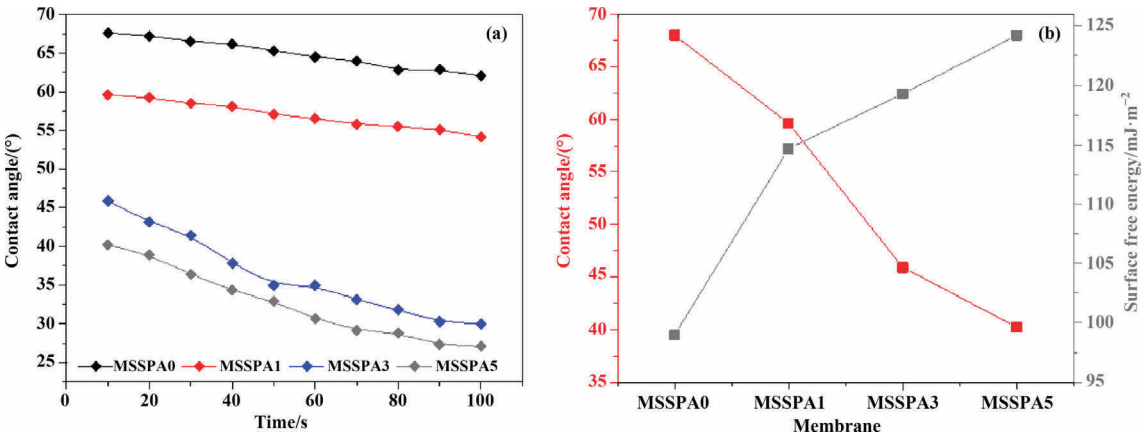

Fig. 7. (a) Dynamic and (b) static contact angles and surface free energy of the pristine and hybrid membranes with various contents of SBA-15-*g*-PSPA.

improved mechanical properties of the fabricated membrane. Consequently, SBA-15 functionalization has responsible to changes in the mechanical characteristics.

3.7. Membrane permeability

Fig. 9(a) and (b) display the measured UF efficiency of the fabricated membranes. It can be seen that by loading 5% (mass) of SBA-15-*g*-PSPA (MSSPA5), the pure water flux was increased dramatically to 402.15 $L{\cdot}m^{-2}{\cdot}h^{-1}$, which is ~1.5 times that of MSSPA0 (268.0 $L{\cdot}m^{-2}{\cdot}h^{-1}$), as shown in Fig. 9(a). Such significantly improved membrane UF efficiency can be determined by (i) the presence of hydroxyl and sulfonic moieties on the membrane surface and water channels resulted in membranes with high hydrophilicity, which is advantageous to water flux; (ii) the membrane porosity was improved with the loading of SBA-15-*g*-PSPA, which is also advantageous for improved water flux [49].

BSA and HA were chosen as model foulants in this research to evaluate the antifouling and filtration efficiency of composite membranes. The flux of foulant solution (BSA or HA) was smaller than the flux of pure water, shown in Fig. 9(b). This could be attributed to the accumulation of foulant on the membrane surface or inside the pores during the UF process at 10^5 Pa pressure [50]. Nevertheless, with the increasing content of SBA-15-*g*-PSPA, the flux of foulant solution was increased monotonically. The aggregation of foulants over the membrane surface MSSPA5 could be inhibited by the strong hydration layer of adsorbed water molecules. The BSA solution flux was less than HA solution flux under identical experimental conditions, possibly due to the higher fouling ability of BSA. For BSA, the highest foulant solution flux was achieved from the MSSPA3 composite membrane, which has the highest porosity and pore radius. Hence, the reduction in the BSA flux is likely associated with the accumulation of BSA within the pores. For HA, the highest foulant solution flux was achieved from the MSSPA5 composite membrane, although it has lower porosity and smaller pore radius with respect to MSSPA3. Hence, by increase the quantity of SBA-15-*g*-PSPA to a certain level, the pore diameter was increased so much that it is no longer affecting the HA solution flux. Meanwhile, the surface potential and surface hydrophilicity were increased further from MSSPA3 to MSSPA5. Therefore, the increased HA foulant solution flux was likely determined by these surface properties, rather than the pore structures. For different membrane, the rates of rejection (*R*, %) for HA, BSA, and SA foulants were quantitatively measured, summarized in Table 3. The pristine membrane (MSSPA0) exhibited the highest rejection ratio in comparison with the composite membranes. This is related to its lower porosity and smaller pore radius, which improves the rejection through the exclusion mechanism of various molecular size, but at the expense of a smaller flux [51].

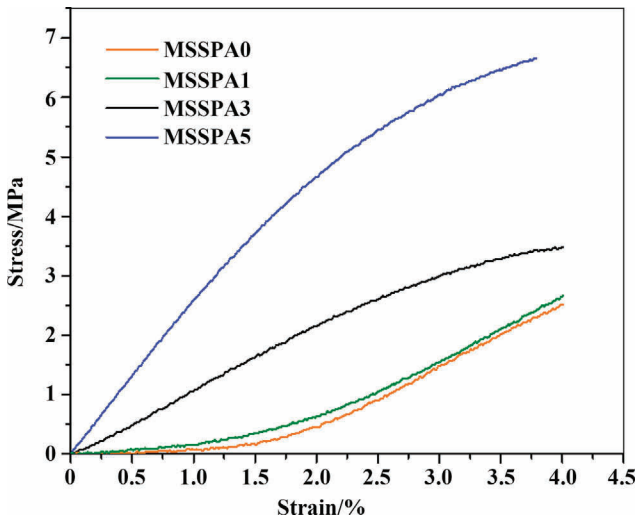

Fig. 8. Stress–strain curves for the pristine and hybrid membranes with various SBA-15-*g*-PSPA contents.

3.8. Membrane antifouling efficiency

The quantity of foulant adsorbed over the membrane surface is an important parameter that determines the service life of the membrane, since the performance of the membrane will suffer from the foulant adsorption. By the increase of SBA-15-*g*-PSPA content, the adsorptions of BSA, HA and SA foulants were all reduced monotonically as shown in Fig. 10(a). For the MSSPA5 membrane, the lowest adsorbed foulant amount was observed (BSA: 59 $\mu g{\cdot}cm^{-2}$, HA: 48 $\mu g{\cdot}cm^{-2}$, and SA: 21 $\mu g{\cdot}cm^{-2}$). This could be attributed to (i) the greatest hydrophilicity of the fabricated membranes allowing the formation of hydration layers, which reduced the adsorption and adhesion of foulants, (ii) the columbic repulsion between the negatively charged foulant species and the increased negative surface potential of the composite membranes [12]. Furthermore, due to the enhanced degree of electrostatic repulsion and the development of a robust hydration layer, the very hydrophilic and effectively negatively charged MSSPA5 membrane (−33 mV) inhibits foulant (BSA, HA, or SA) deposition to a greater extent than the other membranes. The FRR is a parameter indicating the recovery of the UF membrane. As a function of SBA-15-*g*-PSPA amount, the FRR of all membranes were measured (Fig. 10(b)). All the hybrid membranes showed

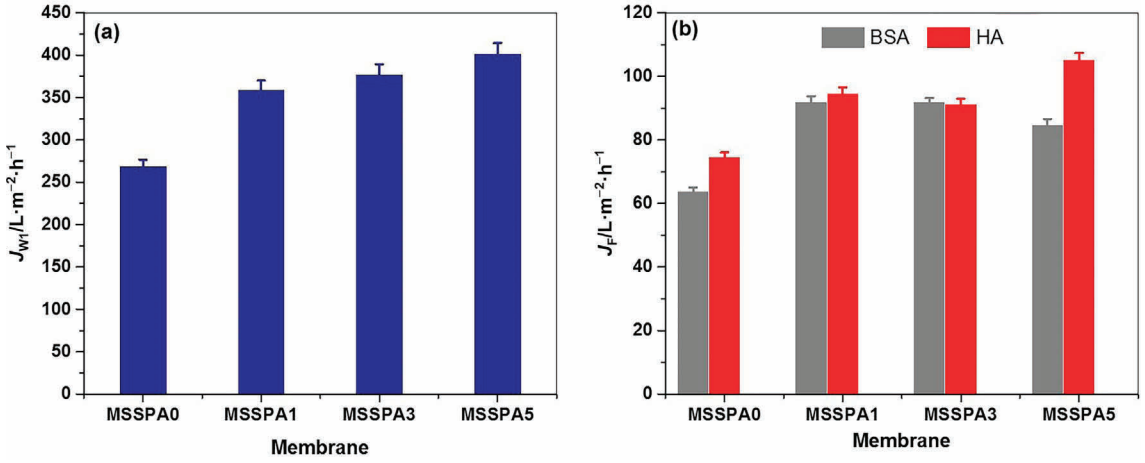

Fig. 9. (a) Pure water and (b) 100 $\mu g{\cdot}g^{-1}$ foulant (BSA and HA) solution flux of the hybrid membranes at pH = 7 and 10^5 Pa.

Table 3
Rejection rate (%) for pristine and fabricated hybrid membranes applied in solution (100 μg·g^{-1}) of HA, BSA, and SA

Membrane	R_{HA}/%	R_{BSA}/%	R_{SA}/%
MSSPA0	98.3 ± 0.3	93.3 ± 0.4	91.9 ± 0.4
MSSPA1	98.1 ± 0.5	92.8 ± 0.5	91.3 ± 0.5
MSSPA3	97.9 ± 0.4	93.5 ± 0.6	89.5 ± 0.4
MSSPA5	97.5 ± 0.3	92.6 ± 0.3	89.6 ± 0.4

much better recovery than that of the pristine membrane. The FRR values increased monotonically with the increase of the SBA-15-*g*-PSPA concentration. The maximum FRR for BSA of 85% was achieved from the MSSPA5 membrane, increased from 53.3% from the MSSPA0 membrane. A similar trend was observed for HA. However, due to the weaker adhesion of HA on the membranes, higher FRR values were recorded, as shown in Fig. 10(b). This indicates that in general, foulants were weakly adsorbed on the highly hydrophilic composite membranes modified with SBA-15-*g*-PSPA. The membrane UF performance can be easily recovered by washing with distilled water and NaOH (0.02 mol·L^{-1}), and the water flux was recovered after washing.

The membranes fouling resistance was also examined applying a feed solution consist of a mixture of NOMs. The tests were conducted *via* UF experiments for 2 h, then the membranes were washed with the alternating of DI water and NaOH (0.02 mol·L^{-1}) for 30 min. From Fig. 11(a), the NOM solution flux was significantly

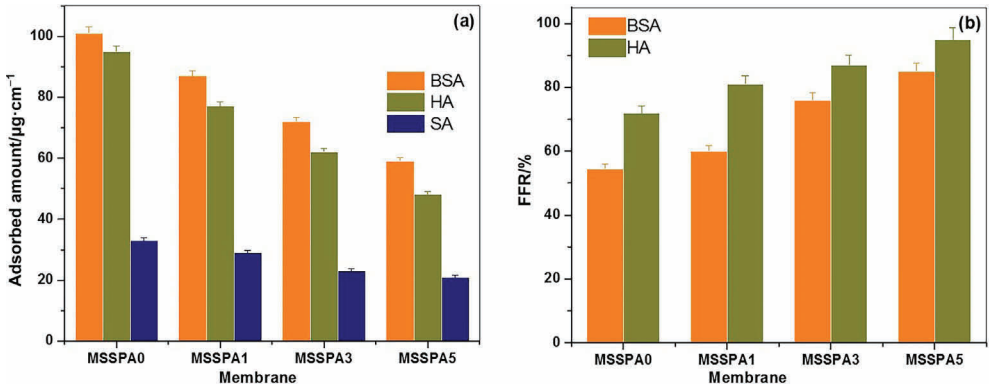

Fig. 10. (a) Adsorbed amount of BSA, HA, and SA per unit area of different membranes and (b) flux recovery ratio (FRR) of the pristine and hybrid membranes.

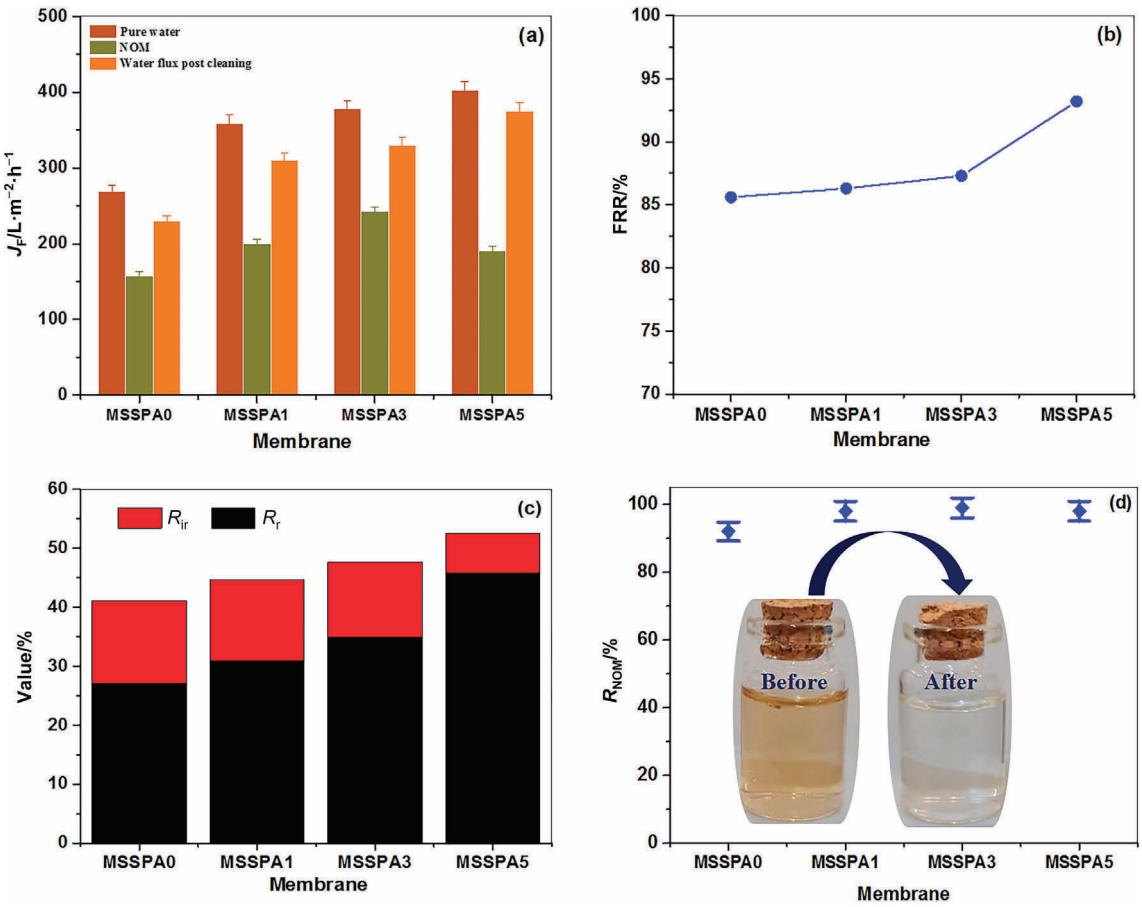

Fig. 11. (a) Pure water, NOM, and water flux after 30 min washing with DI water and 0.02 mol·L^{-1} NaOH solution, (b) FFR, (c) R_r and R_{ir} values, and (d) rejection performance of the membrane (inset represents a NOM solution image before and after UF).

Table 4
Efficient comparison of MSSPA5 membrane and other types of UF membrane

Membranes	Water flux/ $L{\cdot}m^{-2}{\cdot}h^{-1}$	Rejection/ %	FRR/ %	R_{ir}/ %	R_r/%	Reference
PES-1.5	192	92	82.4	17.6	42.9	[40]
MSP1	272	97	94	–	–	[41]
PES/HANTs-DATA	315	87	78	22	47	[52]
PSF	116	95	70	30	34	[53]
PS	118	85	70	30	21	[54]
MSAPSF-7	277	96	78	24	49	[55]
SPPSU-SC20	380	91	92	29	5	[56]
MSSPA5	402	98	94	6.7	46	This work

smaller than that of pure water flux. This may due to the adsorption of NOM foulant components on the outer surface and inside pores of the membranes. However, the NOM flux did increase as the loading of SBA-15-*g*-PSPA increases up to 3% (mass) in the membrane. Further increase of the quantity of SBA-15-*g*-PSPA caused a small drop in NOM flux. Since the hydrophilicity and pore radius increase as the SBA-15-*g*-PSPA, both can be responsible for the improved flux. However, from MSSPA3 to MSSPA5, although the hydrophilicity was further increased, the pore radius was reduced. Hence, the decrease of NOM flux from MSSPA5 suggests that the pore size, rather than the hydrophilicity, is responsible for the NOM flux behavior. From Fig. 11(b), the FRR raised from 63% for MSSPA0 to 97% for MSSPA5. This indicates that the binding of NOM on MSSPA5 was much weaker than the binding on MSSPA0, hence the NOM is easier to be washed off from the MSSPA5 membrane. This confirms that the increased hydrophilic character of the SBA-15-*g*-PSPA filling offered a significant improvement in the fouling resistance to the solution of NOM. R_r, and R_{ir} parameters were also calculated from pure water flux, foulants flux, and post-washing pure water flux of the prepared membranes to high light the antifouling characteristics (Fig. 11(c)). The same trend behavior of R_r values and the reversed trend of R_{ir} values as the FRR further confirm the reversible and weak adsorption of NOM. The rejection ratio for the NOM by the composite membrane is shown in Fig. 11(d). It confirms that all of the synthesized SPES membranes were able to successfully remove the NOM from the aquatic solution, with the best rejection performance exceeding 98% by the composite membrane with 3% (mass) SBA-15-*g*-PSPA. The photograph in (inset in Fig. 9(d)) shows the color of the NOM solution prior and post the UF process utilizing the membrane MSSPA5, visually demonstrating the effectiveness of the prepared membranes of removing NOM from the authentic solution with a rejection performance increasing 98%.

The membranes MSSPA5 was selected for reusability assessment that include fouling with the NOM and washing with DI water. In the first run, the FRR of MSSPA5 membrane was 96.5%. More notably, the FRR of MSSPA5 membrane was still sustained at 93.1% and 89.4% following the second and third fouling and cleaning runs, respectively. For further meaningful comparison, the performance acquired by various membranes are reported in Table 4. As displayed in this Table, the fabricated membrane in the present study has a substantial performance when compared to other membranes [40,41,52–56].

4. Conclusions

In our study, the NIPS approach was successfully used to fabricate novel composite UF SPES membranes with different concentrations of SBA-15-*g*-PSPA additives. The composite membranes offer increased porosity with increased pore radius. The addition of SBA-15-*g*-PSPA also improved the surface hydrophilicity of the membranes. The large pores and high hydrophilicity are responsible for the much improved UF efficiency than the pristine SPES membrane. With the increased amounts of SBA-15-*g*-PSPA, the surface hydrophilicity, the surface charge, and water uptake were all improved, which results in the dramatic increase in the pure water flux with a maximal pure water flux of 402 $L{\cdot}m^{-2}{\cdot}h^{-1}$ from the MSSPA5 membrane. Antifouling efficiency of the composite membranes in the UF of BSA or HA foulants is also drastically improved. Moreover, an excellent rejection ratio of 98% is achieved in the removal of NOM by the composite membranes modified with 3% (mass) of SBA-15-*g*-PSPA. To sum up, this research demonstrates an approach for increasing the hydrophilicity and antifouling efficiency of the hybrid UF membranes without sacrificing their selectivity. This process may also be used to create other hybrid membranes utilizing various different membrane-based polymers and SBA-15 as a nanofiller.

Declaration of Competing Interest

The authors declare that they have no known competing financial interests or personal relationships that could have appeared to influence the work reported in this paper.

Acknowledgements

The authors extend their appreciation to the Deputyship for Research & Innovation, Ministry of Education in Saudi Arabia for funding this research work through the project number (UB-40-1442).

Supplementary Material

Supplementary data to this article can be found online at https://doi.org/10.1016/j.cjche.2021.09.019.

References

[1] X. Liu, H.B. Du, Z.K. Zhang, J.C. Crittenden, M.L. Lahr, J. Moreno-Cruz, D.B. Guan, Z.F. Mi, J. Zuo, Can virtual water trade save water resources?, *Water Res* 163 (2019) 114848.
[2] W. Gao, H. Liang, J. Ma, M. Han, Z.L. Chen, Z.S. Han, G.B. Li, Membrane fouling control in ultrafiltration technology for drinking water production: A review, *Desalination* 272 (1–3) (2011) 1–8.
[3] J.-y. Tian, M. Ernst, F. Cui, M. Jekel, Effect of particle size and concentration on the synergistic UF membrane fouling by particles and NOM fractions, *J. Membr. Sci.* 446 (2013) 1–9.
[4] H. Tabani, S. Nojavan, M. Alexovič, J. Sabo, Recent developments in green membrane-based extraction techniques for pharmaceutical and biomedical analysis, *J. Pharm. Biomed. Anal.* 160 (2018) 244–267.
[5] T. Vu, J. LeBlanc, C.C. Chou, Clarification of sugarcane juice by ultrafiltration membrane: Toward the direct production of refined cane sugar, *J. Food Eng.* 264 (2020) 109682.
[6] J.H. Jhaveri, Z.V.P. Murthy, A comprehensive review on anti-fouling nanocomposite membranes for pressure driven membrane separation processes, *Desalination* 379 (2016) 137–154.
[7] W. Qing, X. Li, S. Shao, X. Shi, J. Wang, Y. Feng, W. Zhang, W. Zhang, Polymeric catalytically active membranes for reaction-separation coupling: A review, *J. Membr. Sci.* 583 (2019) 118–138.
[8] N. Hilal, O.O. Ogunbiyi, N.J. Miles, R. Nigmatullin, Methods employed for control of fouling in MF and UF membranes: A comprehensive review, *Sep. Sci. Technol.* 40 (10) (2005) 1957–2005.
[9] A.G. Fane, C.J.D. Fell, A review of fouling and fouling control in ultrafiltration, *Desalination* 62 (1987) 117–136.
[10] A. Nabe, E. Staude, G. Belfort, Surface modification of polysulfone ultrafiltration membranes and fouling by BSA solutions, *J. Membr. Sci.* 133 (1) (1997) 57–72.
[11] P. Kallem, Y. Ibrahim, S.W. Hasan, P.L. Show, F. Banat, Fabrication of novel polyethersulfone (PES) hybrid ultrafiltration membranes with superior permeability and antifouling properties using environmentally friendly sulfonated functionalized polydopamine nanofillers, *Sep. Purif. Technol.* 261 (2021) 118311.
[12] Z. Liu, Z. Mi, S. Jin, C. Wang, D. Wang, X. Zhao, H. Zhou, C. Chen, The influence of sulfonated hyperbranched polyethersulfone-modified halloysite nanotubes on

the compatibility and water separation performance of polyethersulfone hybrid ultrafiltration membranes, *J. Membr. Sci.* 557 (2018) 13–23.
[13] M.Y. Hu, Z.Y. Cui, S.Q. Yang, J.Y. Li, W.X. Shi, W. Zhang, C. Matindi, B.Q. He, K.J. Fang, J.X. Li, Pregelation of sulfonated polysulfone and water for tailoring the morphology and properties of polyethersulfone ultrafiltration membranes for dye/salt selective separation, *J. Membr. Sci.* 618 (2021) 118746.
[14] T. Tavangar, F.Z. Ashtiani, M. Karimi, Morphological and performance evaluation of highly sulfonated polyethersulfone/polyethersulfone membrane for oil/water separation, *J. Polym. Res.* 27 (9) (2020) 252.
[15] J.J. Zhang, S.W. Chen, J.S. Li, W.Q. Han, X.Y. Sun, N. Li, Z.X. Hu, L.J. Wang, Sulfonated carbon nano-onion incorporated polyethersulfone nanocomposite ultrafiltration membranes with improved permeability and antifouling property, *Sep. Purif. Technol.* 256 (2021) 117825.
[16] L. Zhang, Z. Cui, M. Hu, Y. Mo, S. Li, B. He, J. Li, Preparation of PES/SPSf blend ultrafiltration membranes with high performance *via* H_2O-induced gelation phase separation, *J. Membr. Sci.* 540 (2017) 136–145.
[17] L.M. Bai, Y.T. Liu, A. Ding, N.Q. Ren, G.B. Li, H. Liang, Surface coating of UF membranes to improve antifouling properties: Acomparison study between cellulose nanocrystals (CNCs) and cellulose nanofibrils (CNFs), *Chemosphere* 217 (2019) 76–84.
[18] D. Rana, T. Matsuura, R.M. Narbaitz, C. Feng, Development and characterization of novel hydrophilic surface modifying macromolecule for polymeric membranes, *J. Membr. Sci.* 249 (1-2) (2005) 103–112.
[19] D. Rana, T. Matsuura, R.M. Narbaitz, Novel hydrophilic surface modifying macromolecules for polymeric membranes: Polyurethane ends capped by hydroxy group, *J. Membr. Sci.* 282 (1–2) (2006) 205–216.
[20] Y. Kim, D. Rana, T. Matsuura, W.-J. Chung, Influence of surface modifying macromolecules on the surface properties of poly(ether sulfone) ultrafiltration membranes, *J. Membr. Sci.* 338 (1-2) (2009) 84–91.
[21] Y. Kim, D. Rana, T. Matsuura, W.-J. Chung, K.C. Khulbe, Relationship between surface structure and separation performance of poly(ether sulfone) ultrafiltration membranes blended with surface modifying macromolecules, *Sep. Purif. Technol.* 72 (2) (2010) 123–132.
[22] D. Rana, Y. Kim, T. Matsuura, H.A. Arafat, Development of antifouling thin-film-composite membranes for seawater desalination, *J. Membr. Sci.* 367 (1-2) (2011) 110–118.
[23] Y. Kim, D. Rana, T. Matsuura, W.-J. Chung, Towards antibiofouling ultrafiltration membranes by blending silver containing surface modifying macromolecules, *Chem. Commun.* 48 (5) (2012) 693–695.
[24] D. Rana, B. Scheier, R.M. Narbaitz, T. Matsuura, S. Tabe, S.Y. Jasim, K.C. Khulbe, Comparison of cellulose acetate (CA) membrane and novel CA membranes containing surface modifying macromolecules to remove pharmaceutical and personal care product micropollutants from drinking water, *J. Membr. Sci.* 409-410 (2012) 346–354.
[25] D. Rana, R.M. Narbaitz, A.-M. Garand-Sheridan, A. Westgate, T. Matsuura, S. Tabe, S.Y. Jasim, Development of novel charged surface modifying macromolecule blended PES membranes to remove EDCs and PPCPs from drinking water sources, *J. Mater. Chem. A* 2 (26) (2014) 10059–10072.
[26] D.J. Miller, D.R. Dreyer, C.W. Bielawski, D.R. Paul, B.D. Freeman, Surface modification of water purification membranes, *Angew. Chem. Int. Ed.* 56 (17) (2017) 4662–4711.
[27] J. Shen, S. Shahid, A. Sarihan, D.A. Patterson, E.A.C. Emanuelsson, Effect of polyacid dopants on the performance of polyaniline membranes in organic solvent nanofiltration, *Sep. Purif. Technol.* 204 (2018) 336–344.
[28] X. Fang, J. Li, B. Ren, Y. Huang, D. Wang, Z. Liao, Q. Li, L. Wang, D.D. Dionysiou, Polymeric ultrafiltration membrane with *in situ* formed nano-silver within the inner pores for simultaneous separation and catalysis, *J. Membr. Sci.* 579 (2019) 190–198.
[29] L. Qi, Z. Liu, N. Wang, Y. Hu, Facile and efficient *in situ* synthesis of silver nanoparticles on diverse filtration membrane surfaces for antimicrobial performance, *Appl. Surf. Sci.* 456 (2018) 95–103.
[30] N. Song, X.L. Gao, Z. Ma, X.J. Wang, Y. Wei, C.J. Gao, A review of graphene-based separation membrane: Materials, characteristics, preparation and applications, *Desalination* 437 (2018) 59–72.
[31] D. Ji, C. Xiao, S. An, J. Zhao, J. Hao, K. Chen, Preparation of high-flux PSF/GO loose nanofiltration hollow fiber membranes with dense-loose structure for treating textile wastewater, *Chem. Eng. J.* 363 (2019) 33–42.
[32] M. Golpour, M. Pakizeh, Preparation and characterization of new PA-MOF/PPSU-GO membrane for the separation of KHI from water, *Chem. Eng. J.* 345 (2018) 221–232.
[33] T. Yang, H. Xiong, F. Liu, Q. Yang, B. Xu, C. Zhan, Effect of UV/TiO_2 pretreatment on fouling alleviation and mechanisms of fouling development in a cross-flow filtration process using a ceramic UF membrane, *Chem. Eng. J.* 358 (2019) 1583–1593.
[34] A. Hassanpour, S. Nahar, X. Tong, G.X. Zhang, M.A. Gauthier, S.H. Sun, Photocatalytic interlayer spacing adjustment of a graphene oxide/zinc oxide hybrid membrane for efficient water filtration, *Desalination* 475 (2020) 114174.
[35] Y. Liu, R. Wei, O. Lin, W. Zhang, Y. Du, C. Wang, C. Zhang, Enhanced hydrophilic and antipollution properties of PES membrane by anchoring SiO_2/HPAN nanomaterial, *ACS Sustain. Chem. Eng.* 5 (9) (2017) 7812–7823.
[36] X. Li, T. Zhao, Y. Lu, P. Wang, A.M. El-Toni, F. Zhang, D. Zhao, Degradation-restructuring induced anisotropic epitaxial growth for fabrication of asymmetric diblock and triblock mesoporous nanocomposites, *Adv. Mater.* 29 (30) (2017) 1701652.
[37] M.A. Betiha, H.M.A. Hassan, A.M. Al-Sabagh, A.E.R.S. Khder, E.A. Ahmed, Direct synthesis and the morphological control of highly ordered mesoporous AlSBA-15 using urea-tetrachloroaluminate as a novel aluminum source, *J. Mater. Chem.* 22 (34) (2012) 17551–17559.
[38] A. Martín, J.M. Arsuaga, N. Roldán, J. de Abajo, A. Martínez, A. Sotto, Enhanced ultrafiltration PES membranes doped with mesostructured functionalized silica particles, *Desalination* 357 (2015) 16–25.
[39] Y. Orooji, F. Liang, A. Razmjou, G. Liu, W. Jin, Preparation of anti-adhesion and bacterial destructive polymeric ultrafiltration membranes using modified mesoporous carbon, *Sep. Purif. Technol.* 205 (2018) 273–283.
[40] Q. Li, S. Pan, X. Li, C. Liu, J. Li, X. Sun, J. Shen, W. Han, L. Wang, Hollow mesoporous silica spheres/polyethersulfone composite ultrafiltration membrane with enhanced antifouling property, *Colloids Surf. A: Physicochem. Eng. Aspects* 487 (2015) 180–189.
[41] H. Wang, X. Lu, D. Lu, P. Wang, J. Ma, Development of a high-performance polysulfone hybrid ultrafiltration membrane using hydrophilic polymer-functionalized mesoporous SBA–15 as filler, *J. Appl. Polym. Sci.* 136 (18) (2019) 47353.
[42] A. Razvan, D.F. Popa, O. Oprea, E. Vasile, F. Dumitru, G. Nechifor, Ultrafiltration mixed matrix membranes based on mesoporous silica (MCM-41, HMS) embedded in polysulfone, *Rev. Chim.* 70 (9) (2019) 3089–3093.
[43] Z.H. Si, Z. Wang, D. Cai, G.Z. Li, S.F. Li, P.Y. Qin, A high-permeance organic solvent nanofiltration membrane via covalently bonding mesoporous MCM-41 with polyimide, *Sep. Purif. Technol.* 241 (2020) 116545.
[44] M. Kumar, N. Sreedhar, M.A. Jaoude, H.A. Arafat, High-flux, antifouling hydrophilized ultrafiltration membranes with tunable charge density combining sulfonated poly(ether sulfone) and aminated graphene oxide nanohybrid, *ACS Appl. Mater. Interfaces* 12 (1) (2020) 1617–1627.
[45] L. Bai, H. Liang, J. Crittenden, F. Qu, A.n. Ding, J. Ma, X. Du, S. Guo, G. Li, Surface modification of UF membranes with functionalized MWCNTs to control membrane fouling by NOM fractions, *J. Membr. Sci.* 492 (2015) 400–411.
[46] H.X. Feng, R.M. Wang, Y.F. He, Z.Q. Lei, Y.P. Wang, C.G. Xia, J.S. Suo, Preparation and catalysis of porous silica supported metal Schiff-base complex, *J. Mol. Catal. A: Chem.* 159 (1) (2000) 25–29.
[47] K.M. Parida, S. Singha, P.C. Sahoo, A facile method for promoting activities of vanadium-schiffbase complex anchored on organically modified MCM-41 in epoxidation reaction, *J. Mol. Catal. A: Chem.* 325 (1–2) (2010) 40–47.
[48] A. Martín, J.M. Arsuaga, N. Roldán, A. Martínez, A. Sotto, Effect of amine functionalization of SBA-15 used as filler on the morphology and permeation properties of polyethersulfone-doped ultrafiltration membranes, *J. Membr. Sci.* 520 (2016) 8–18.
[49] Q.-Z. Zheng, P. Wang, Y.-N. Yang, Rheological and thermodynamic variation in polysulfone solution by PEG introduction and its effect on kinetics of membrane formation *via* phase-inversion process, *J. Membr. Sci.* 279 (1–2) (2006) 230–237.
[50] L. Zhang, J. Xu, Y. Tang, J. Hou, L. Yu, C. Gao, A novel long-lasting antifouling membrane modified with bifunctional capsaicin-mimic moieties *via in situ* polymerization for efficient water purification, *J. Mater. Chem. A* 4 (26) (2016) 10352–10362.
[51] P.H.H. Duong, V.A. Kuehl, B. Mastorovich, J.O. Hoberg, B.A. Parkinson, K.D. Li-Oakey, Carboxyl-functionalized covalent organic framework as a two-dimensional nanofiller for mixed-matrix ultrafiltration membranes, *J. Membr. Sci.* 574 (2019) 338–348.
[52] Y. Mu, K. Zhu, J. Luan, S. Zhang, C. Zhang, R. Na, Y. Yang, X.i. Zhang, G. Wang, Fabrication of hybrid ultrafiltration membranes with improved water separation properties by incorporating environmentally friendly taurine modified hydroxyapatite nanotubes, *J. Membr. Sci.* 577 (2019) 274–284.
[53] A. Khan, T.A. Sherazi, Y. Khan, S. Li, S.A.R. Naqvi, Z. Cui, Fabrication and characterization of polysulfone/modified nanocarbon black composite antifouling ultrafiltration membranes, *J. Membr. Sci.* 554 (2018) 71–82.
[54] Y. Pan, Z. Yu, H. Shi, Q.i. Chen, G. Zeng, H. Di, X. Ren, Y.i. He, A novel antifouling and antibacterial surface-functionalized PVDF ultrafiltration membrane *via* binding Ag/SiO_2nanocomposites, *J. Chem. Technol. Biotechnol.* 92 (3) (2017) 562–572.
[55] Y.Y. Wang, H.C. Shen, C.F. Cui, L. Hou, W.B. Chen, Q. Liu, J.M. Xu, Z. Wang, J.L. Hu, Towards to better permeability and antifouling sulfonated poly (aryl ether ketone sulfone) with carboxyl group ultrafiltration membrane blending with amine functionalization of SBA-15, *Sep. Purif. Technol.* 265 (2021) 118512.
[56] D.i. Zhou, G. Rong, S.a. Huang, J. Pang, Preparation of a novel sulfonated polyphenlene sulfone with flexible side chain for ultrafiltration membrane application, *Sep. Purif. Technol.* 210 (2019) 817–823.